energies

MDPI

Article

Radiation Heat Transfer in a Complex Geometry Containing Anisotropically-Scattering Mie Particles

Ali Ettaleb [1], Mohamed Ammar Abbassi [1], Habib Farhat [2], Kamel Guedri [3], Ahmed Omri [1], Mohamed Naceur Borjini [4], Marjan Goodarzi [5,*] and M. M. Sarafraz [6]

1 Unité de Recherche «Matériaux, Energie et Energies Renouvelables» (MEER), Faculté des Sciences de Gafsa, B.P.19-2112 Zarroug-Gafsa, Tunisie; alietaleb@gmail.com (A.E.); MedAmmar.Abbassi@enim.rnu.tn (M.A.A.); omri.ahmed233@gmail.com (A.O.)

2 Laboratoire des Etudes des Milieux Ionisés et Réactifs Avenue Ibn-Eljazzar, 5019 Monastir, Tunisie; habibfarhat@ipeim.rnu.tn

3 Mechanical Engineering Department, College of Engineering and Islamic Architecture, Umm Al-Qura University, Makkah 21955, Saudi Arabia; kamel.guedri@enim.rnu.tn

4 Unité de Métrologie et des Systèmes Energétiques, Ecole Nationale d'Ingénieurs de Monastir, Université de Monastir, 5000 Monastir, Tunisie; naceur.borjini@issat.rnu.tn

5 Sustainable Management of Natural Resources and Environment Research Group, Faculty of Environment and Labour Safety, Ton Duc Thang University, Ho Chi Minh City, Vietnam

6 School of Mechanical Engineering, University of Adelaide, Adelaide SA 5005, South Australia, Australia; mohammadmohsen.sarafraz@adelaide.edu.au

* Correspondence: marjan.goodarzi@tdtu.edu.vn; Tel.: (+1)-502-432-0339

Received: 7 September 2019; Accepted: 16 October 2019; Published: 19 October 2019

check for updates

Abstract: This study aims to numerically investigate the radiation heat transfer in a complex, 3-D biomass pyrolysis reactor which is consisted of two pyrolysis chambers and a heat recuperator. The medium assumes to be gray, absorbs, emits, and Mie-anisotropically scatters the radiation energy. The finite volume method (FVM) is applied to solve the radiation transfer equation (RTE) using the step scheme. To treat the complex geometry, the blocked-off-region procedure is employed. Mie equations (ME) are applied to evaluate the scattering phase function and analyze the angular distribution of the anisotropically scattered radiation by particles. In this study, three different states are considered to test the anisotropic scattering impacts on the temperature and radiation heat flux distribution. These states are as: (i) Isotropic scattering, (ii) forward and backward scattering and (iii) scattering with solid particles of different coals and fly ash. The outcomes demonstrate that the radiation heat flux enhances by an increment of the albedo and absorption coefficients for the coals and fly ash, unlike the isotropic case and the forward and backward scattering functions. Moreover, the particle size parameter does not have an important influence on the radiation heat flux, when the medium is thin optical. Its effect is more noticeable for higher extinction coefficients.

Keywords: radiation; blocked-off-region procedure; heat recuperation; anisotropic scattering; mie particles

1. Introduction

For a vast range of engineering applications, radiation is a substantial method of heat transfer. Especially, in high temperature equipment like furnaces, boilers, gas turbine combustors, and nuclear reactors, where the combustion generating luminous flames includes combustion gases and other particles. Where the scattering is mostly anisotropic, the particles emit, absorb and scatter radiant energy. Therefore, the necessity for analysis of radiation heat transfer leads to an increase demand for developing well-designed radiation models, applicable to arbitrary shaped multi-dimensional geometries and capable of treating anisotropic characteristics in participating media. In recent decades, many researchers have tried to calculate the radiation transfer equation (RTE) in multidimensional complicated geometries. Considering computation costs and precision, three most adopted methods could be recalled the discrete transfer, the discrete ordinates and the finite-volume methods. The first description of the discrete transfer method (DTM) is presented by Lockwood and Shah [1] and applied later to complex geometries by the cell-blocking process according to Cartesian coordinates [2], and nonorthogonal grid systems [3]. Chai et al. [4] used the DOM with the blocked-off-region procedure. Fiveland and Jesse [5] have accomplished a formulation of the discrete ordinates method (DOM) using finite element associated with curvilinear grids. The finite volume method (FVM) was adapted with various procedures that treated the problem of irregular geometries. The FVM was developed with nonorthogonal coordinate systems [6], the blocked-off-region [7–9], and the spatial-multiblock [10] procedures. Coelho et al. [11] modelled the radiation heat transfer in enclosures including blocks of narrow thicknesses by the above-mentioned methods. Guedri et al. [12] investigated the impacts of baffles on radiation heat transfer in the 2-D and 3-D complicated geometries. The authors examined two different schemes: The STEP and CLAM schemes. Furthermore, they treated the effect of change of the absorption and albedo coefficients on the temperature profiles as well as net radiation heat flux distributions in a 3-D biomass pyrolysis reactor. The similar study is done by Abbassi et al. [13] in a 2-D complex geometry. They examined the baffles shadow and soot volume fraction impacts on the temperature profiles and radiation heat flux. In all previous works, the problem of anisotropic scattering is processed in a simple way. Mengüç and Viskanta [14] analyzed the radiation exchanges in a 3-D rectangular enclosure housing radiatively participating mixture of gases and anisotropic scattering particles applying the first and third-order spherical harmonics approximation. The delta-Eddington model is employed to define the scattering phase function. Kim and Lee [15,16] studied the impact of the anisotropic scattering in a 2-D rectangular enclosure using the S-N discrete ordinates scheme. The scattering phase function is expanded in a series of Legendre polynomials. Results indicated that the phase function anisotropy has a vital importance in the radiation heat transfer while the non-symmetric boundary conditions are considered in the problem. Farmer and Howell [17] used the Monte Carlo approach to anticipate the radiation heat transfer within general inhomogeneous media that represents both highly spectral and anisotropic scattering behaviors. Guo and Maruyama [18] investigated the scaled isotropic scattering radiation in a 3-D inhomogeneous medium by the radiation element method. In a 2-D rectangular enclosure, Trivic et al. [19–21] coupled the FVM to calculate the radiation transfer equation employing Mie equations for evaluating the scattering phase function. This model can be applied to any given particle parameters regardless the previous designed analytical expressions for the scattering function. It is also adopted for the radiation heat transfer in a 3-D geometry with grey and non-grey anisotropically scattering media. In this work, the authors used two different numerical schemes to solve the radiation transfer equation: (i) The finite volume method with a highly refined angular discretization and (ii) the combination of zone method and the Monte Carlo statistical simulation method, and for the non-gray gases, they used the Smith's weighted sum of gray gases model (WSGGM) for a hypothetical gas represented by 5 gray gases. Outcomes from the two methods are found in an acceptable agreement. Hunter and Guo [22] presented a technique for the normalization of the phase function to meet the scattered energy conservation constraint and thus, minimize the numerical errors generated by the discretization of the integral numerical term in the RTE. This technique is simpler and applied to the 3-D FVM to enhance radiation calculation precision and efficiency in anisotropically scattering media. The outcomes matched well to those achieved by the Monte Carlo and discrete-ordinates methods for a cubic enclosure confining a highly-anisotropic scattering mediumproblem. The authors achieved an acceptable compromise between the FVM results by applying the normalization technique, and the two different methods by little effect on computational efficiency. Guedri et al. [23] formulated and applied the FTn Finite Volume Method (FTn FVM) for transient radiation in a 3-D absorbing, emitting, and anisotropically scattering medium. The outcomes illustrated that FTn FVM decreases mostly the ray impacts and its accuracy is higher than the standard FVM. Moreover, FTn FVM has shorter convergence time compared to the standard FVM for all cases using both STEP and CLAM schemes.

The aim of this study is to understand the anisotropic scattering phenomenon impact on the radiation heat transfer in a 3-D complex geometry. The enclosure is a pilot plant for biomass pyrolysis reactor consisted of two pyrolysis chambers and a heat recuperator. The FVM is used in relation to the blocked-off-region process and Mie equations to evaluate the scattering phase function (SPF). The heat recuperator includes a gray, absorbing–emitting, and anisotropically scattering medium. Solid particles of many different coals and fly ash are formed during the pyrolysis process. The main advantage of the proposed procedure is that it can be readily applied to radiating particles of any types within the Mie scattering approximation limits, given the geometrical and optical particle parameters like the complicated index of refraction, wavelength of the incident radiation and particle mean diameter.

2. Mathematical Formulations

2.1. Radiation Transfer Equation

In this study, an absorbing, emitting and anisotropically scattering gray medium, comprising of a mixture of gas and particles inside an enclosure is considered. For such a situation, the integro-differential radiation transfer equation (RTE) is given by [6]:

$$\frac{dI(\vec{r},\vec{\Omega})}{ds} = -\beta(\vec{r})I(\vec{r},\vec{\Omega}) + S(\vec{r},\vec{\Omega}) \tag{1}$$

The RTE resulting from an energy balance performed for a volume element, means that radiation intensity along a given path $\vec{\Omega}$ gaines radiation energy by absorption and in-scattering but decreases by emission and out-scattering of radiation energy.

$\beta(\vec{r})$ and $S(\vec{r},\vec{\Omega})$ are respectively the local extinction coefficient and source function given by

$$\beta(\vec{r}) = \kappa(\vec{r}) + \sigma(\vec{r}) \tag{2a}$$

$$S(\vec{r},\vec{\Omega}) = \kappa(\vec{r})I_b(\vec{r}) + \frac{\sigma(\vec{r})}{4\pi}\int_{4\pi} I(\vec{r},\vec{\Omega})\Phi(\vec{\Omega},\vec{\Omega}')d\Omega' \tag{2b}$$

The radiation intensity $I(\vec{r},\vec{\Omega})$ depends on the Cartesian coordinates (x, y, z) of the position vector $\vec{r}$, and the polar and azimuthal angles (θ, ϕ), that characterise the radiant intensity direction, defined by the unit vector

$$\vec{\Omega} = \sin\theta\cos\phi\,\vec{e}_x + \sin\theta\sin\phi\,\vec{e}_y + \cos\theta\,\vec{e}_z \tag{3}$$

The FVM is used to discretize the RTE. This method comprises of dividing the computational area into $N_x \times N_y \times N_z$ control volumes and the spherical space into $N_\theta \times N_\phi$ control solid angles. The initial solid angle is analytically computed by

$$\Delta\Omega^l = \int_{\theta^{l-}}^{\theta^{l+}} \int_{\phi^{l-}}^{\phi^{l+}} \sin\theta d\theta d\phi \tag{4}$$

The following finite volume formula may be achieved by considering the constant magnitude of the radiation intensity and varying its orientation through the control volume and control angle.

$$\sum_m I_m^l \Delta A_m N_{c,i}^l = (-\beta I^l + S^l)\Delta V_P \tag{5}$$

where

$$N_{c,i}^{l} = \frac{1}{\Delta\Omega^{l}} \int_{\Delta\Omega^{l}} (\vec{\Omega}^{l} \cdot \vec{n}_i) d\Omega^{l} \tag{6}$$

Equation (7) is achieved using the STEP scheme which is obtained by Chai et al. [24] in 3D discretization.

$$a_P^l I_P^l = a_W^l I_W^l + a_E^l I_E^l + a_S^l I_S^l + a_N^l I_N^l + a_F^l I_F^l + a_R^l I_R^l + b_P^l \tag{7}$$

where

$$a_I^l = \Delta A_m \| -N_{c,m}^l, 0 \|, \text{ I} = \text{W, E, S, N, F and R}$$

$$a_P^l = \sum_m \Delta A_m \| N_{c,m}^l \|, 0 + \beta \Delta V_P$$

$$b_P^l = S^l \Delta V_P$$

$$S^l = \kappa I_b + \frac{\sigma}{4\pi} \sum_{l'=1}^{L} I_P^{l'} \overline{\Phi}^{ll'} \Delta\Omega$$

The quantity $\overline{\Phi}^{l'l}$ is defined as the average scattering phase function (ASPF) from control angle l' (incident angle) to control angle l (scattering angle). It is expressed as follows

$$\overline{\Phi}^{l'l} = \frac{\int_{\Delta\Omega^{l}} \int_{\Delta\Omega^{l'}} \Phi(\vec{\Omega}^{l}, \vec{\Omega}^{l'}) d\Omega^{l} d\Omega^{l'}}{\Delta\Omega^{l} \Delta\Omega^{l'}} \tag{8a}$$

$\overline{\Phi}^{l'l}$ can be estimated by the previous equation discretization [25]

$$\overline{\Phi}^{l'l} = \frac{\sum_{l_s=1}^{L_s} \sum_{l'_s=1}^{L'_s} \Phi^{l'_s l_s} \Delta\Omega^{l'_s} \Delta\Omega^{l_s}}{\Delta\Omega^{l} \Delta\Omega^{l'}} \tag{8b}$$

where $\Delta\Omega^{l'_s}$ and $\Delta\Omega^{l_s}$ are the sub-control angles.

The radiant intensities are calculated as follows

$$I_P^l = \frac{a_W^l I_W^l + a_E^l I_E^l + a_S^l I_S^l + a_N^l I_N^l + a_F^l I_F^l + a_R^l I_R^l + b_P^l}{a_P^l} \tag{9}$$

When the below convergence criterion is satisfied, the iterative procedure is terminated for all cases:

$$\frac{\left| I_P^l - I_P^{l_0} \right|}{I_P^l} \leq 10^{-5} \tag{10}$$

where l_0 and l stand for the previous and current iterations, respectively.

2.2. Boundary Conditions

The radiation boundary conditions are defined by the below equation for a gray, diffusely reflecting, opaque, and emitting surface:

$$I(\vec{r}, \vec{\Omega}) = \varepsilon(\vec{r}) I_b(\vec{r}) + \frac{\rho(\vec{r})}{\pi} \int_{\vec{n}.\vec{\Omega}'<0} I(\vec{r}, \vec{\Omega}) \left| \vec{\Omega}'.\vec{n} \right| d\Omega' \tag{11a}$$

The following equation represents the discretized form of Equation (11).

$$I^l = \varepsilon_w I_b + \frac{\rho_w}{\pi} \sum_{l'} I^{l'} N_w^{l'} \Delta\Omega^{l'} \tag{11b}$$

2.3. Scattering Phase Function

The phase function describes the angular distribution of the scattered radiation which is denoted by Φ. This function illustrates the possibility that an incident ray beam centered around the direction $\vec{\Omega}'$, is scattered towards the propagation direction $\vec{\Omega}$.

In the spherical particle size compared with the incident beam wavelength ($x_p \approx 1$), the Mie theory applies and thus, the anisotropic scattering incident is described by the phase function described by [26]

$$\Phi(\Theta) = 2\frac{i_1 + i_2}{x_p^2 Q_{sca}} \tag{12}$$

Θ represents the scattering angle between the incomingand the outgoing directions respectively $\vec{\Omega}$ and $\vec{\Omega}'$, evaluated using the following expression

$$\cos\Theta = \mu\mu' + (1-\mu^2)^{1/2}(1-\mu'^2)\cos(\varphi' - \varphi) \tag{13}$$

(i_1, i_2) are the non-dimensional polarized intensities; Q_{sca} is the efficiency factor for scattering and x_p is the particle size parameter. In this study, the value of x_p is dependent on wavelength and the particle radius, it is used to calculate the typical wavelength of λ = 3.1415 µm as suggested by Modest [27]. Indeed, the definition of Mie theory equations for homogeneous spherical particles, and all the appropriate variables linked to Equation (12) are represented in detail by [19]. The iterative calculations will be stopped as indicated by Deirmendjian et al. [26], when $n = 1.2x_p + 9$.

3. Blocked-Off-Region Procedure

The blocked-off-region process is consisted of appending artificial areas to the real physical domain to gain a simple formation where the RTE solution is very simple to create. This process has been expanded for conduction and convection heat transfer, and after that, developed to radiation transfer by Chai et al. [6,7] and Borjini et al. [8].

An extra source term is added to discern real areas from artificial ones as follows:

$$S_{bloc} = S_C + S_P I_P^l \tag{14}$$

The extra source term is chosen for a specified black boundary as follows: $(S_C, S_P) = (0,0)$ and $(MI_b, -M)$ for the real areas and the fictitious ones, respectively. Curved and inclined shapes can be dealt with applying this process by a grid mesh refinement.

4. Validation

To validate our implemented numerical code prior to its application for case study problems (i.e., 3-D complex geometry), the results of Trivic and Amon [20] are used. The authors solved the RTE by combining the zone (ZM) and Monte Carlo (MC) solution methods where the SPF is described by Mie Equations (ME). The utilized software in this research is coded using the FORTRAN computing language.

A cubic enclosure with a length of 1.0 is considered. The calculation area is discretized into (15 × 15 × 15) uniform control volumes, and (16 × 20) control solid angle. The rear wall is black and hot with $E_{br} = 1$. All the other walls are assumed to be black and cold. The enclosure confines a pure scattering medium with $\beta = 1\ \text{m}^{-1}$. In this section, the quantities are non-dimensional. It is noted that X= x/L, Y= y/L and Z= z/L are the non-dimensional coordinates and L is the cube side.

Four various states are investigated: One isotropic with the designation ISO and three anisotropic states with the scattering phase functions denoted with F1, B1, and carbon [19].

All the particle information which is used to evaluate the scattering phase functions F1 and B1 are taken from [28] and presented in Table 1. Letters F and B denote the forward and backward-directed scattering phase functions, respectively.

Table 1. Data for evaluation of the scattering phase functions by Mie equations.

Scattering Phase Function	F1	B1
Particle size parameter x_p	5	1
Real part of complex refractive index n	1.33	very large, taken 10^8
Imaginary part of complex refractive index k	0	0

The variation of the considered scattering phase functions versus the scattering angle are demonstrated in Figure 1a,b. It is shown that the scattered radiation by fly ash particles for small particle size parameter presents a similar tends as B1 phase function. As x_p increases, the scattered radiation tends to be directed towards the forward direction. F1 phase function seems to be adequate to represent the fly ash scattering behavior when $x_p = 5$.

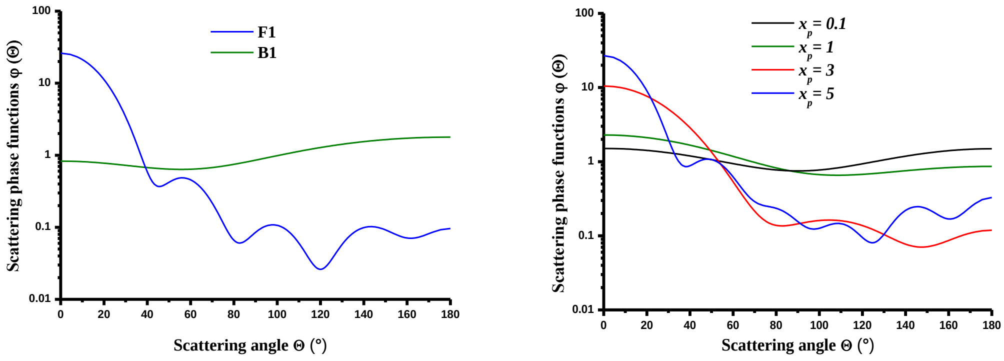

(**a**) (**b**)

Figure 1. Scattering phase functions: (**a**) Function F1 and B1, (**b**) fly ash for different size parameters.

Figure 2a–c presents the net radiation heat flux density in **y** direction $q^*_{ys} = q_{ys}/E$ at the middle of bottom wall, along the z coordinate. The (FVM + ME) predictions corresponding to the isotropic case (Figure 2a) and carbon (Figure 2d), clearly follows the (ZM + MC) results. Figure 2b depicts that the F1 function predictions for function F1 of the heat flux with (FVM + ME) follow those obtained with the aid of (ZM+MC). The maximum discrepancy observed does not exceed 26%. For the scattering function B1, the achieved result is underestimated compared with benchmark.

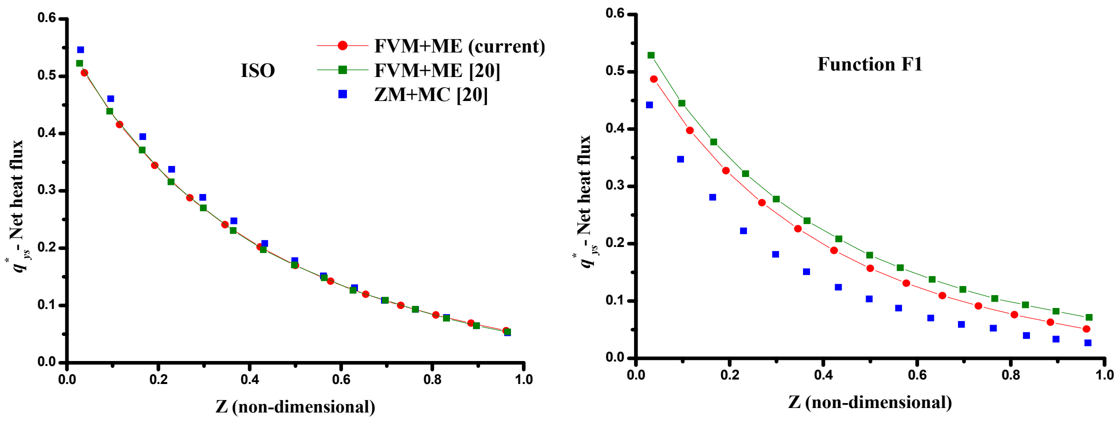

(**a**) (**b**)

Figure 2. *Cont.*

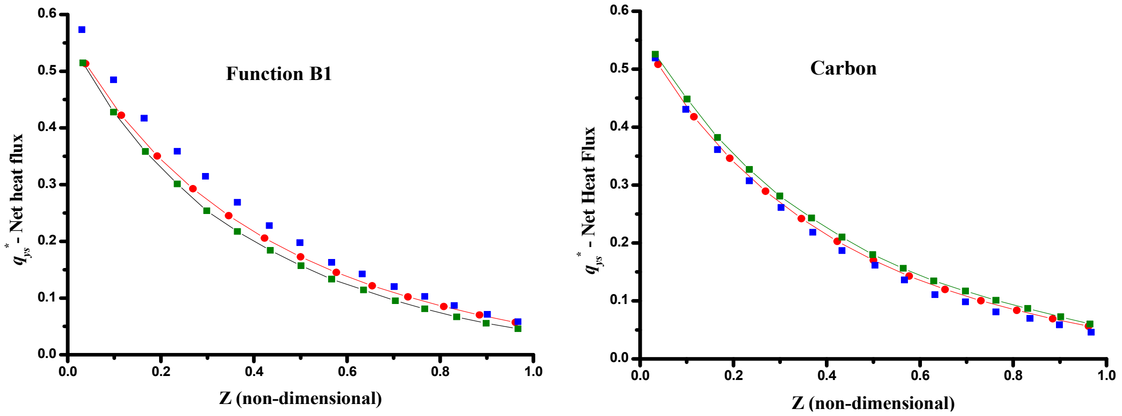

(c) **(d)**

Figure 2. Dimensionless radiation heat flux density in y-direction at the middle of south wall (X= 0.5, Y= 0.0).

The z-component of the dimensionless net radiation heat flux density $q_{zf}^* = q_{zf}/E$, at the middle of the cold front wall, along x-coordinate is shown in Figure 3a–c. First, the isotropic case, shown in Figure 3a presents an overestimation around 10.8% for the (FVM+ME) results as compared with the (ZM + MC) solutions. In Figure 3b, where the case of function F1 is shown, our results present an overestimation around 39% with benchmark (ZM + MC). Figure 3c shows the (FVM+ME) results corresponding to B1 phase function which agree well with the reference predictions. Figure 3d presents the (FVM+ME) predictions for carbon, and shows an overestimation ranging between 18.2% and 21.3%.

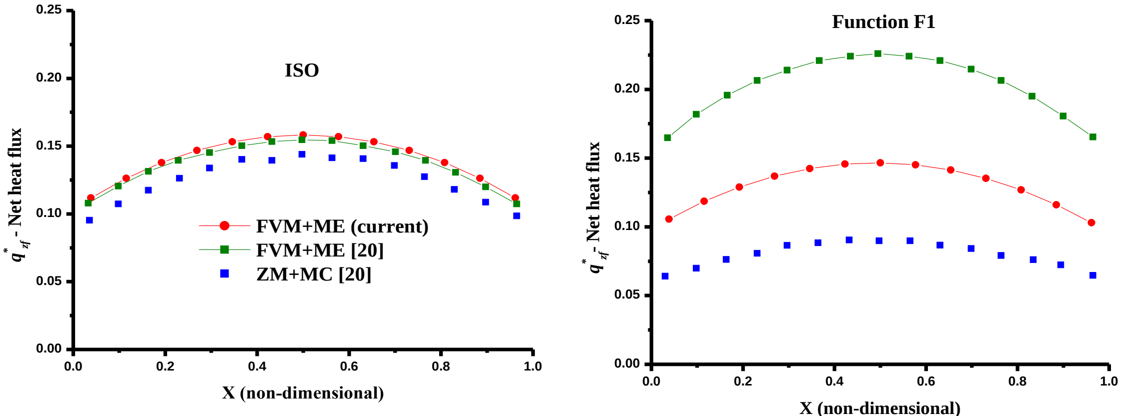

(a) **(b)**

Figure 3. *Cont.*

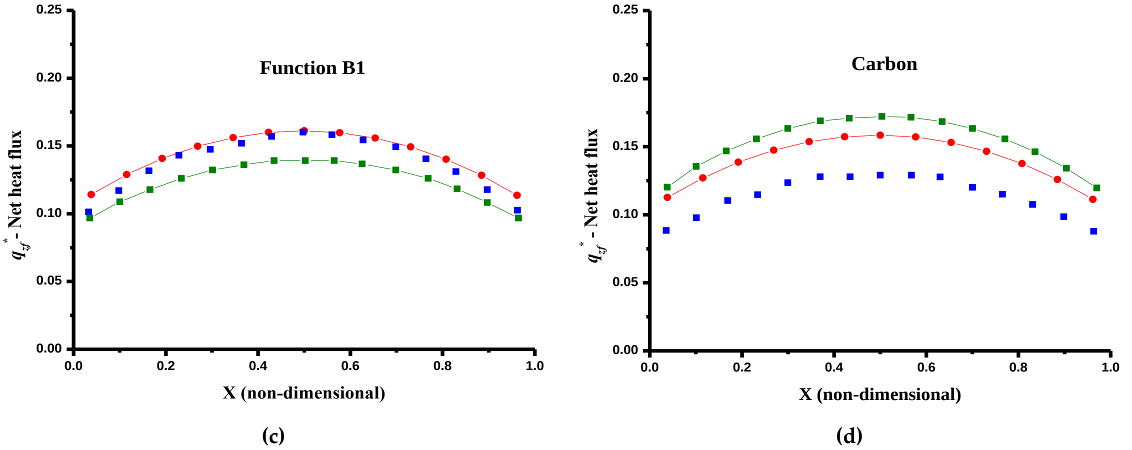

Figure 3. Dimensionless radiation heat flux density in *z*-direction at the middle of front cold wall (Y= 0.5, Z= 1.0).

It should be noted that the results found by Trivic and Amon [20], using the FVM for the resolution of the RTE and ME for evaluating the scattering phase function, are also shown on the previous figures.

5. A 3D Complex Heat Recuperator of Biomass Pyrolysis Fumes

The biomass pyrolysis pilot plant is composed of two metallic rooms for biomass pyrolysis and a heat recuperator, as described in detail by Abbassi et al. [12,13,28] (Figure 4a,b).The heat recuperator consists of a parallelepiped metallic construction with dimensions (1.8, 1.2, 1.2) m, including two cylindrical chambers and 17 baffles in direct contact with gases emitted from the combustion of biomass pyrolysis fumes.

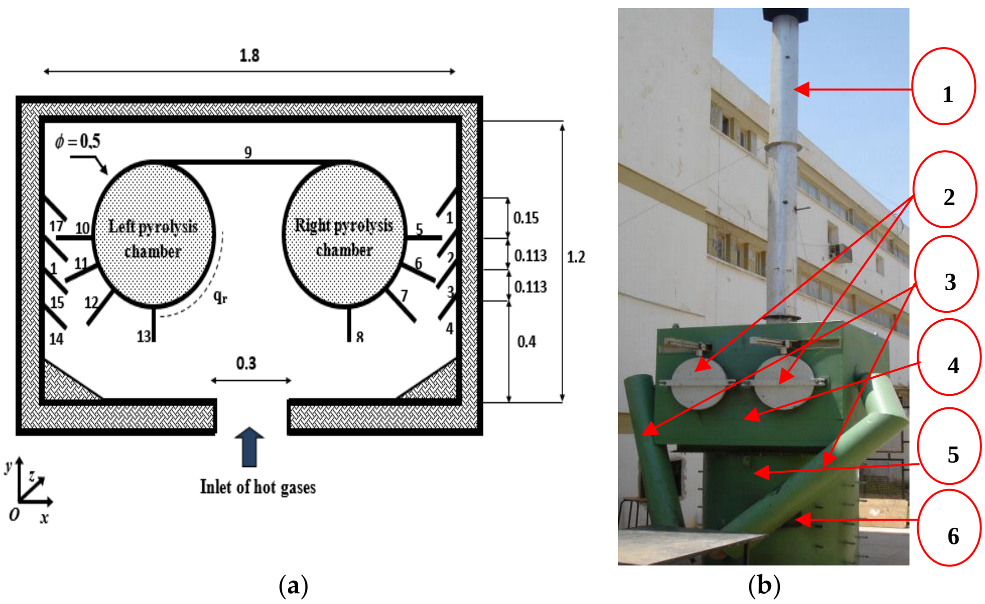

Figure 4. (**a**) Geometrical characteristics of the heat recuperator projected in *z*-plane, (**b**) Pilot plan. 1. Chimney. 2. Pyrolysis chambers. 3. Pyrolysis gases channels. 4. Heat exchanger. 5. Pyrolysis gases combustor. 6. Pyrolysis gases and air combustor inlet.

6. Result and Discussion

6.1. Grid Independence

The heat recuperator contains an absorbing-emitting and anisotropically scattering medium. The temperature of all the walls was evaluated equal to 300 K with an emissivity equal to $\epsilon = 0.8$, except the wall at $y = 0$ and for $0.75 < x < 1.05$ m, where the temperature was assumed 1000 K with a blackbody surface. The baffles are black and were taken at a prescribed temperature of 300 K. The two pyrolysis chambers are considered as black and at a uniform temperature 500 K. This choice is made based on experimental measurements.

In this section, it is aimed to examine the effect of varying the spatial and angular meshes for the isotropic case. The step scheme is employed for all calculations. First, a spatial grid refinement is made as $(N_x \times N_y \times N_z) = (46 \times 44 \times 11)$, $(62 \times 58 \times 11)$, $(92 \times 86 \times 11)$, and $(184 \times 172 \times 11)$, for a fixed angular grid $(N_\theta \times N_\phi) = (4 \times 20)$. The choice of the grid mesh $(92 \times 86 \times 11)$, offers a satisfactory compromise between accuracy and computation time. Also, the number of control solid angles is varied as $(N_\theta \times N_\phi) = (4 \times 12)$, (4×20), (4×24), and (4×20) for the retained spatial grid.It is noted that it does not have a great effect on the CPU time, and consequently, a grid of the type $(N_\theta \times N_\phi) = (4 \times 20)$ seems to be appropriate.

In the following, it is set out to investigate the impact of the scattering anisotropy of particles, the absorption and scattering albedo coefficients on the gas temperature and net radiation flux distributions. The solution method of the RTE for the pilot plant of Figure 4a,b is (FVM+ME). To achieve this, the forward and backward scattering phase functions (F1, B1) are considered. Also, the predictions are analyzed for real engineering fuels and fly ash. The particles are consisting of carbon, anthracite, bituminous and lignite.

6.2. Absorption Coefficient and Scattering Albedo Effects

In this section, a comparison between isotropic and two anisotropic scattering functions (F1, carbon) is made. Figure 5a–g shows the temperature contours at plane *z = 0.6* m, for six cases. It should be mentioned that the size parameter for carbon is $x_p = 1$. First, for an absorption coefficient $\kappa = 1$ m^{-1} (states 1,3, and 5), when the albedo coefficient is relatively weak (i.e., $\omega = 0.1$), it is observed that the temperatures distributions have the same pattern for the two-phase functions: Isotropic case as well as carbon. The impact of scattering anisotropy is negligible, as it refers to an optically thin body with little scattering. Furthermore, it is seen that higher temperatures are distributed near the inlet of the hot-gases region, and at the vicinity of the baffles while the temperature distribution tends to be uniform in the recuperator core region. When the albedo increases, it is seen that the temperature near the lateral baffles remains nearly constant (i.e., 700 K). In the rest of the recuperator, the difference between the temperature contours of the two phase functions is clear. This difference is pronounced with a larger albedo coefficient. For carbon, it can be noted that the isothermal line 700 K (in bold) tends towards the central region. Also, the temperature increases near the horizontal baffle and the cold wall. However, for the isotropic case, contours behavior is completely the opposite. This may be due to the fact that radiation is equally scattered while carbon scattering phase function seems to be a backward-directed function. For an absorption coefficient $\kappa = 5$ m^{-1} (cases 2, 4 and 6), on the one hand, it can be seen a remarkable deformation of the isothermal lines close to the inlet of the hot gases, towards the right pyrolysis room for carbon case especially when $\omega = 0.9$. In addition, there is an increase of the temperature namely in the centre of the recuperator and at the horizontal baffle. On the other hand, for the isotropic case, there is a decline of the temperature in the physical system mainly for a large value of the albedo coefficient, and it is shown a stagnation zone with the highest albedo coefficient, where the temperature about 410 K. In fact, in these regions, the thermal inertia is important, and radiation thermal energy tends to be stored. This phenomenon is perceived when the absorption and the albedo coefficients are high enough.

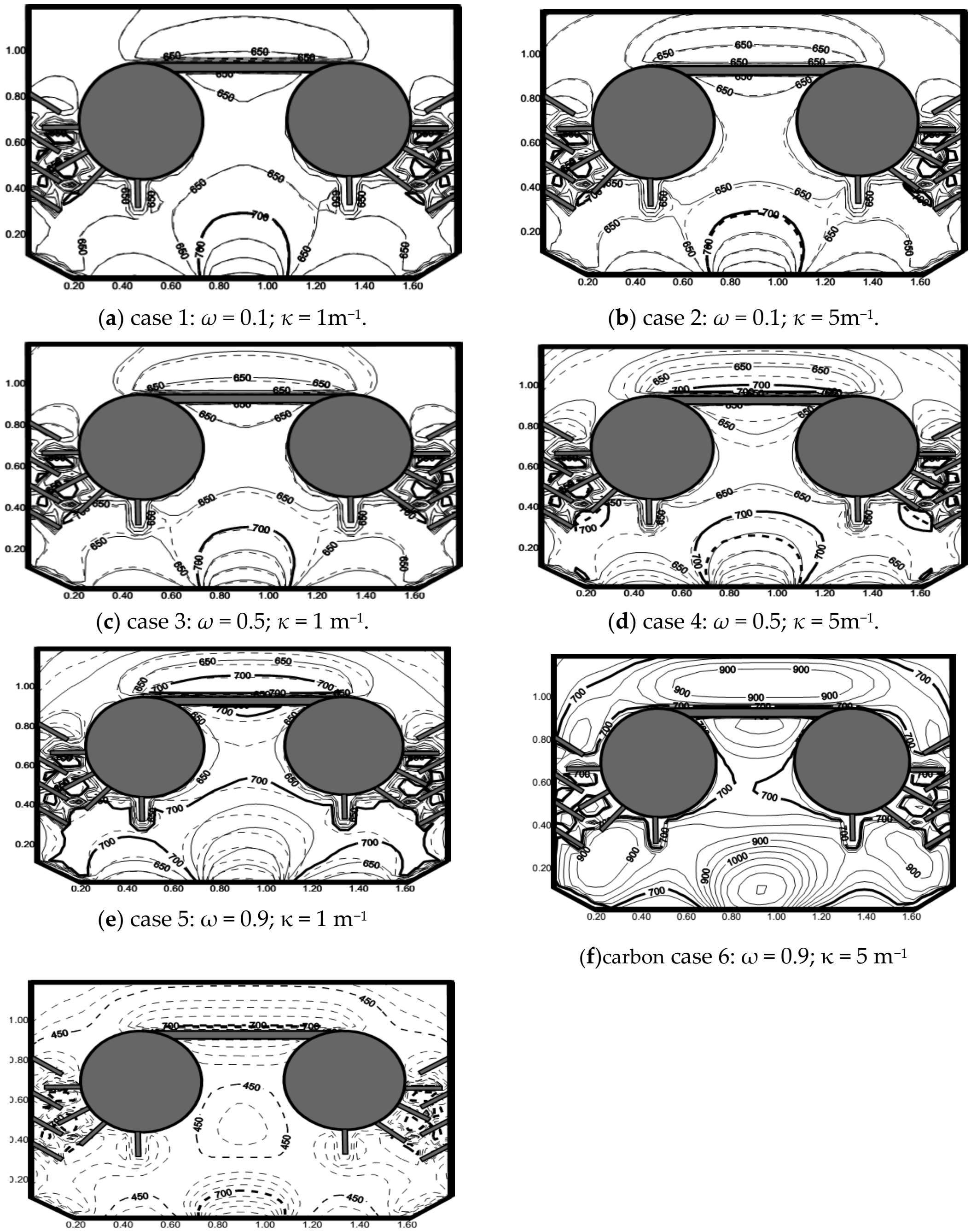

(**a**) case 1: $\omega = 0.1$; $\kappa = 1\mathrm{m}^{-1}$.

(**b**) case 2: $\omega = 0.1$; $\kappa = 5\mathrm{m}^{-1}$.

(**c**) case 3: $\omega = 0.5$; $\kappa = 1\ \mathrm{m}^{-1}$.

(**d**) case 4: $\omega = 0.5$; $\kappa = 5\mathrm{m}^{-1}$.

(**e**) case 5: $\omega = 0.9$; $\kappa = 1\ \mathrm{m}^{-1}$

(**f**)carbon case 6: $\omega = 0.9$; $\kappa = 5\ \mathrm{m}^{-1}$

(**g**) isotropic case 6: $\omega = 0.9$; $\kappa = 5\ \mathrm{m}^{-1}$

Figure 5. Effects of the absorption and albedo coefficients on the medium temperature pattern: Comparison between the isotropic case and carbon. Dashed lines: Isotropic, continuous lines: carbon. (**a**) case 1: $\omega = 0.1$; $\kappa = 1\ \mathrm{m}^{-1}$, (**b**) case 2: $\omega = 0.1$; $\kappa = 5\ \mathrm{m}^{-1}$, (**c**) case 3: $\omega = 0.5$; $\kappa = 1\ \mathrm{m}^{-1}$, (**d**) case 4: $\omega = 0.5$; $\kappa = 5\ \mathrm{m}^{-1}$, (**e**) case 5: $\omega = 0.9$; $\kappa = 1\ \mathrm{m}^{-1}$, (**f**) carbon case 6: $\omega = 0.9$; $\kappa = 5\ \mathrm{m}^{-1}$, (**g**) isotropic case 6: $\omega = 0.9$; $\kappa = 5\ \mathrm{m}^{-1}$.

Figure 6a–g depicts the forecasted net radiation heat flux density contours. For all cases of carbon, it is shown that the radiant energy is directly from the hot regions to the cold ones, and the radiation heat flux is enhanced in all the regions of the recuperator and reachesa maximum value equal 61.47 kW·m^{-2}. For the isotropic case, there is a remarkable fall of the radiation heat flux mainly at the inlet of hot gases with a maximum value of 33.82 kW·m^{-2}. Moreover, the appearance of stagnation zones is noticed for two states.

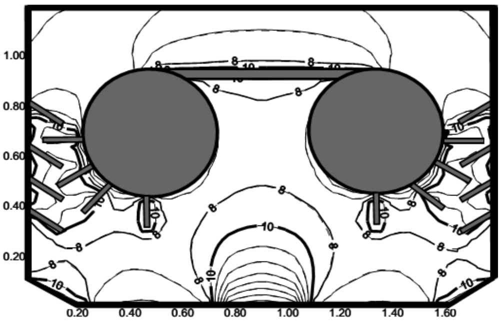

(a) case 1: $\omega = 0.1$; $\kappa = 1\ m^{-1}$.

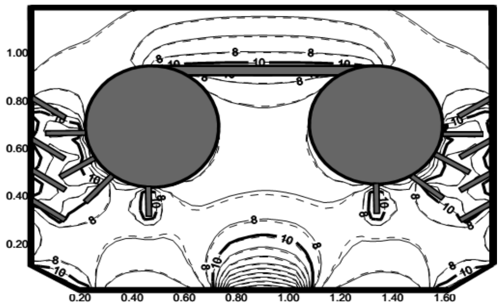

(b) case 2: $\omega = 0.1$; $\kappa = 5 m^{-1}$.

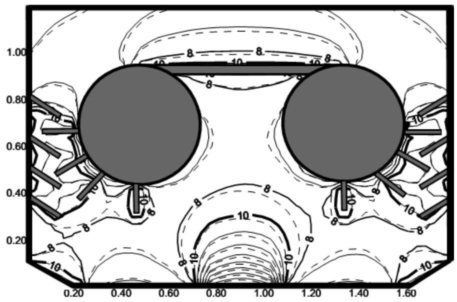

(c) case 3: $\omega = 0.5$; $\kappa = 1 m^{-1}$.

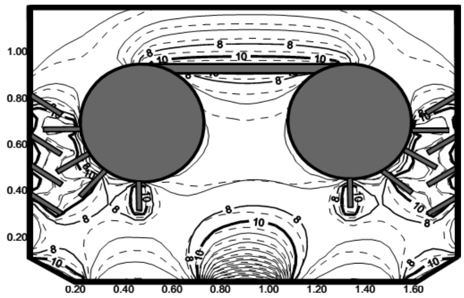

(d) case 4: $\omega = 0.5$; $\kappa = 5\ m^{-1}$.

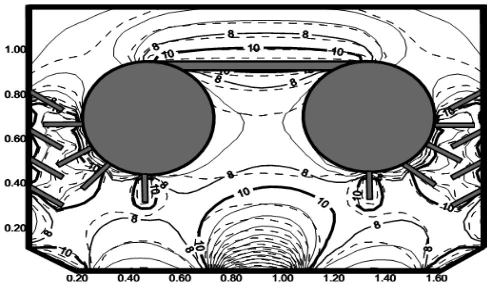

(e) case 5: $\omega = 0.9$; $\kappa = 1\ m^{-1}$.

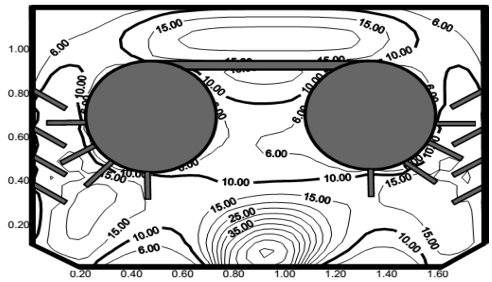

(f) carbon case6: $\omega = 0.9$; $\kappa = 5\ m^{-1}$

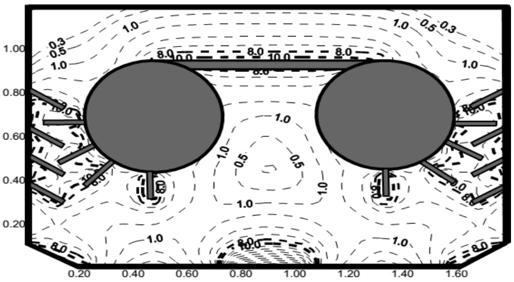

(g) isotropic case 6: $\omega = 0.9$; $\kappa = 5\ m^{-1}$

Figure 6. Effects of the absorption and albedo coefficients on the net radiation heat flux density distribution. Dashed lines: Isotropic, continuous lines: carbon. (**a**) case 1: $\omega = 0.1$; $\kappa = 1\ m^{-1}$, (**b**) case 2: $\omega = 0.1$; $\kappa = 5\ m^{-1}$, (**c**) case 3: $\omega = 0.5$; $\kappa = 1\ m^{-1}$, (**d**) case 4: $\omega = 0.5$; $\kappa = 5\ m^{-1}$, (**e**) case 5: $\omega = 0.9$; $\kappa = 1\ m^{-1}$, (**f**) carbon case 6: $\omega = 0.9$; $\kappa = 5\ m^{-1}$, (**g**) isotropic case 6: $\omega = 0.9$; $\kappa = 5\ m^{-1}$.

Figure 7a–g gives the isothermal lines for the function F1 and the isotropic case. It can be noticed that for the lower amount of the albedo coefficient, the anisotropy effect is imperceptible. As the albedo coefficient increases, a shift of the isotherms is observed corresponding to F1 function as compared to those of the isotropic case and the medium cools down. Also, a deformation of the isotherms is noted, which are close to the inlet of hot gases, toward the right pyrolysis chamber. This that the propagation of radiation is privileged to the right direction this behavioris more important when the absorption coefficient is greater.

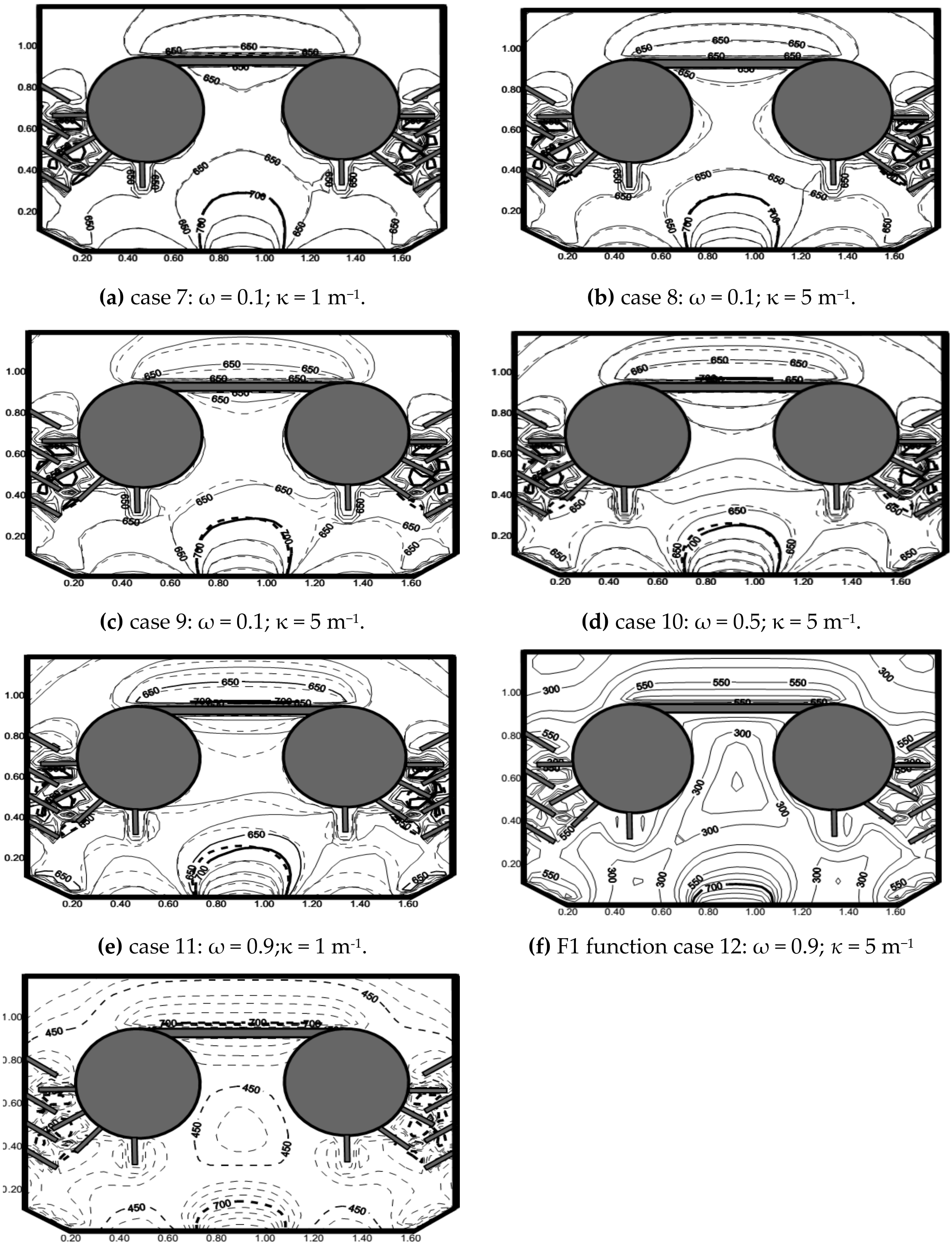

(a) case 7: ω = 0.1; κ = 1 m^{-1}.

(b) case 8: ω = 0.1; κ = 5 m^{-1}.

(c) case 9: ω = 0.1; κ = 5 m^{-1}.

(d) case 10: ω = 0.5; κ = 5 m^{-1}.

(e) case 11: ω = 0.9;κ = 1 m^{-1}.

(f) F1 function case 12: ω = 0.9; κ = 5 m^{-1}

(g) isotropic case 12: ω = 0.9; κ = 5 m^{-1}

Figure 7. Effects of the absorption and albedo coefficients on the medium temperature pattern: Comparison between the isotropic case and F1 function. Dashed lines: Isotropic, continuous lines: carbon. (**a**) case 7: ω = 0.1; κ = 1 m^{-1}, (**b**) case 8: ω = 0.1; κ = 5 m^{-1}, (**c**) case 9: ω = 0.1; κ = 5 m^{-1}, (**d**) case 10: ω = 0.5; κ = 5 m^{-1}, (**e**) case 11: ω = 0.9; κ = 1 m^{-1}, (**f**) F1 function case 12: ω = 0.9; κ = 5 m^{-1}, (**g**) isotropic case 12: ω = 0.9; κ = 5 m^{-1}.

Figure 8a–g shows the net radiation heat flux density contours for F1 and isotropic function. It can be seen that the radiation energy has conducted to the hot area when the absorption and albedo coefficients increase, especially for the anisotropic case. Moreover, a stagnation zone with an unrealistic net radiation heat flux value of –0.25 kW·m^{-2} is seen, indeed, an artificial environment is studied. Furthermore, it should be pointed that the average temperature and net radiation heat flux gradually decrease as the albedo coefficient enhances for the isotropic state and function F1, while they increase for the carbon case due to the backward scattering behavior of carbon particles. Tables 2 and 3 summarize the aforementioned results and also, include results for function B1.

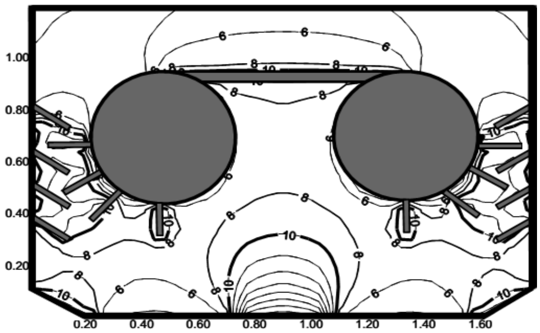

(a) case 7: ω = 0.1; κ = 1 m^{-1}.

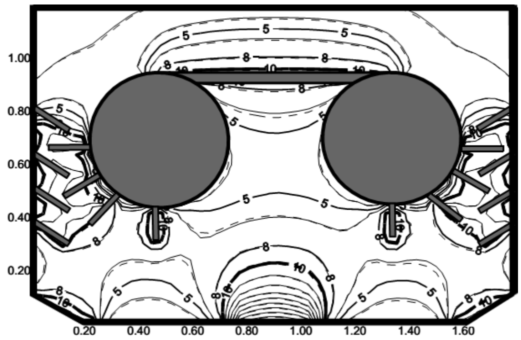

(b) case 8: ω = 0.1; κ = 5 m^{-1}.

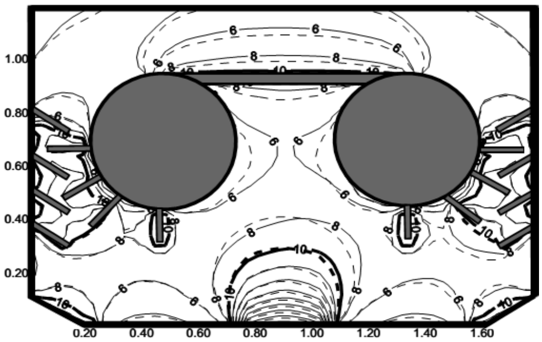

(c) case 9: ω = 0.5; κ = 1 m–1.

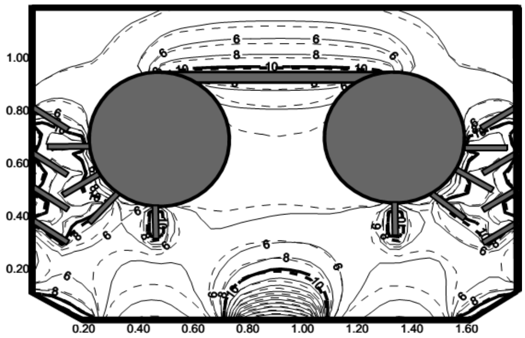

(d) case 10: ω = 0.5;κ = 5 m–1.

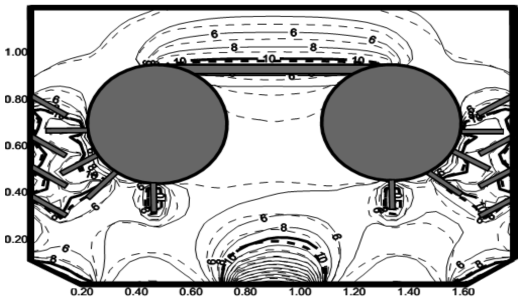

(e) case 11: ω = 0.9; κ = 1 m^{-1}.

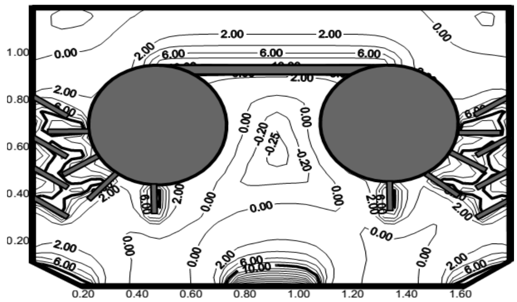

(f) F1 function case 12: ω = 0.9; κ = 5 m^{-1}

Figure 8. *Cont*.

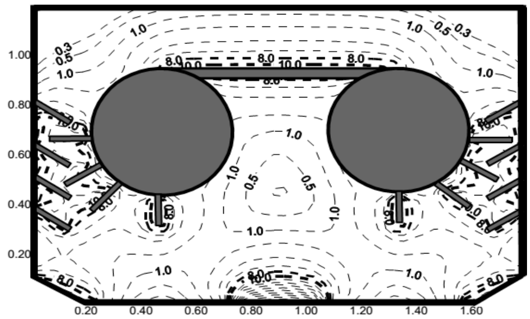

(g) isotropic case 12: ω = 0.9; κ = 5m $^{-1}$

Figure 8. Effects of the absorption and albedo coefficients on the net radiation heat flux density distribution. Dashed lines: Isotropic, continuous lines: carbon. (**a**) case 7: ω = 0.1; κ = 1 m^{-1}, (**b**) case 8: ω = 0.1; κ = 5 m^{-1}, (**c**) case 9: ω = 0.5; κ = 1 m^{-1}, (**d**) case 10: ω = 0.5; κ = 5 m^{-1}, (**e**) case 11: ω = 0.9; κ = 1 m^{-1}, (**f**) F1 function case 12: ω = 0.9; κ = 5 m^{-1}, (**g**) isotropic case 12: ω = 0.9; κ = 5 m $^{-1}$.

Table 2. Average temperature and net radiation heat flux density value for different albedo values (κ = 1 m^{-1}).

Albedo		**ω = 0.1**	**ω = 0.5**	**ω = 0.7**	**ω = 0.9**
ISO	T_{Av} (K)	585.10	585.01	584.29	577.00
	q_{Av} (kW·m^{-2})	6.60	6.43	6.21	5.47
B1	T_{Av} (K)	585.12	585.16	584.37	575.19
	q_{Av} (kW·m^{-2})	6.60	6.46	6.25	5.51
F1	T_{Av} (K)	585.25	585.39	583.12	558.34
	q_{Av} (kW·m^{-2})	6.60	6.45	6.19	5.07
Carbon	T_{Av} (K)	585.50	588.68	593.27	619.60
	q_{Av} (kW·m^{-2})	6.62	6.61	6.62	7.12

Table 3. Average temperature and net radiation heat flux density value for different albedo values (κ = 5 m^{-1}).

Albedo		**ω = 0.1**	**ω = 0.5**	**ω = 0.7**	**ω = 0.9**
ISO	T_{Av} (K)	582.29	577.00	567.71	523.15
	q_{Av} (kW·m^{-2})	5.90	5.47	5.03	4.00
B1	T_{Av} (K)	582.26	576.04	564.54	510.53
	q_{Av} (kW·m^{-2})	5.91	5.5	5.03	3.84
F1	T_{Av} (K)	581.54	565.83	538.07	438.71
	q_{Av} (kW·m^{-2})	5.88	5.21	4.44	2.84
Carbon	T_{Av} (K)	584.47	598.97	623.96	724.18
	q_{Av} (kW·m^{-2})	5.99	6.25	6.92	11.75

It is observed that for $\kappa = 5$ m^{-1}, the anisotropic character has a little effect on the average temperature and net radiation heat flux with a weak albedo coefficient (i.e., $\omega = 0.1$). When varying the albedo from $\omega = 0.1$ to $\omega = 0.9$, the average net radiation heat flux diminishes of 35.02% for the backward function, and 51.70% for the forward function. Actually, the size parameter of F1 function is greater than that of the B1 function, which explains the increase of the scattered energy. Furthermore, one can state that the medium temperature and flux are more sensitive to scattering rather than absorption phenomena. However, it can be seen carbon particles have a reverse effect as compared to the previous phase functions. This behavior is mainly due to the imaginary part of the complex index that is responsible of absorption of radiation. More radiation heat is transferred to the recuperator medium implies less boundary heat losses.

The graphs presented in Figure 9a–c describe the radiation heat flux density q_r on the walls of the left pyrolysis room (Figure 4a) for z = 0.60 m, where the same conditions as previously are considered. It is presented that the wall radiation heat flux density enhances, when approaching the horizontal baffle due to the latter blocks the radiation energy between the two pyrolysis rooms. Moreover, for the lower value of the ω, the anisotropic scattering character is negligible. When increasing ω from 0.1 to 0.9, the carbon phase function enhances the radiation heat emit from the hot surface, whereas the forward and backward scattering phase functions try to decrease it. It is noticed an overprediction of 42.50% for the carbon and an underprediction equal to 20.34% for function F1 as compared to the isotropic case. Yet, the impact of the backward-scattering phase function is found relatively less than the forward-scattering function, regarding the isotropic scattering state. This is foreseeable as forward scattering accentuates the radiation heat exchange between surface and volume zones.

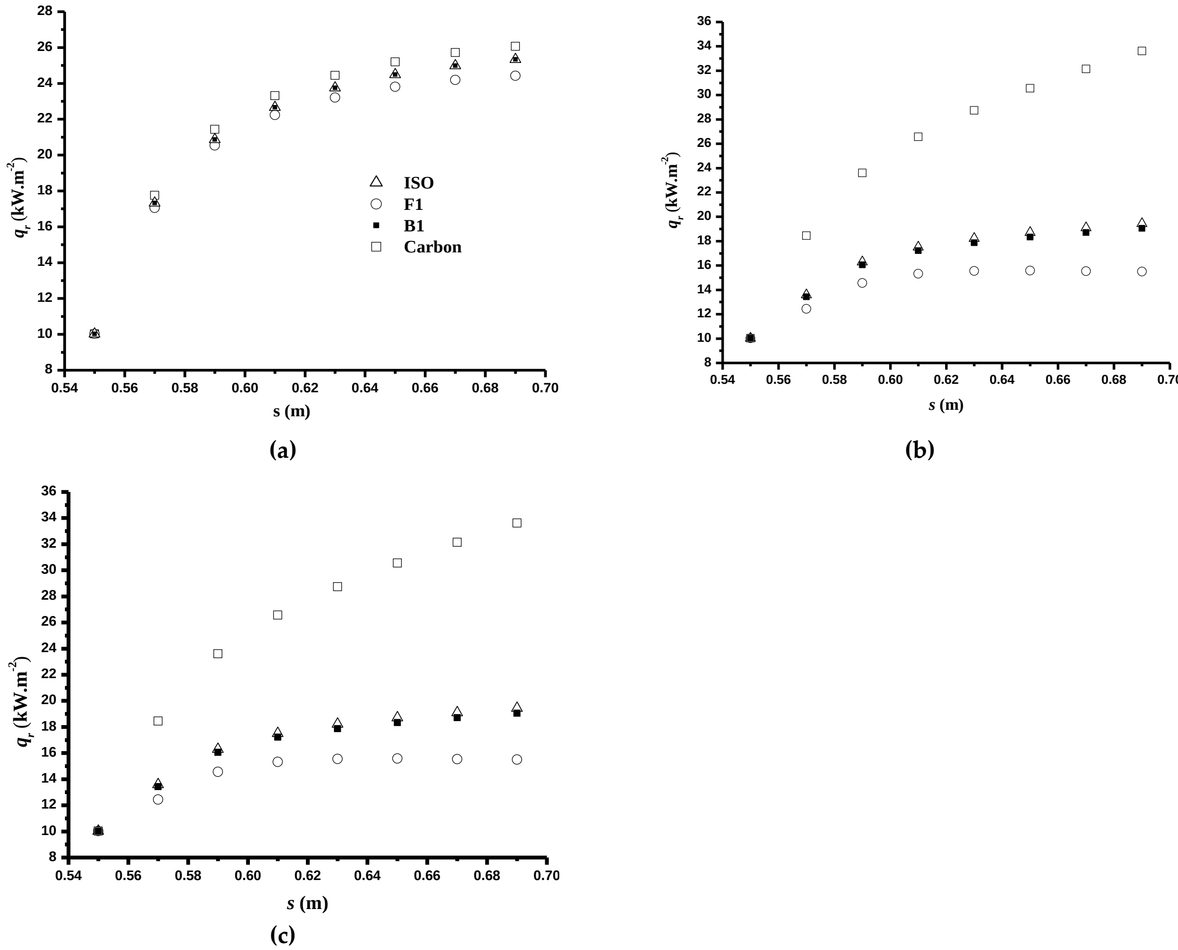

Figure 9. Distributions of the net radiation heat flux density profils on the walls of the left pyrolysis room (z = 0.6 m, κ = 1 m^{-1}): (**a**) ω = 0.1, (**b**) ω = 0.5, (**c**) ω = 0.9.

6.3. Particles Type Effect

The effect of the fly ash and other coals like anthracite, bituminous and lignite on the net radiation flux density contours at the front wall z = 0 mis analyzed. Table 4 are listed the corresponding data for evaluating of scattering phase functions related to the near infrared region [28].

Table 4. Complex refractive index for different coals and ashes in-near infrared region.

Coal and Ash	Carbon	Anthracite	Bituminous	Lignite	Ash
Particle size parameter x_p	1	1	1	1	1
Real part of complex refractive index n	2.20	2.05	1.85	1.70	1.50
Imaginary part of complex refractive index k	1.120	0.540	0.220	0.066	0.020

Numerical results in Figure 10a–d are calculatedfor an absorption coefficient $\kappa = 5\ \mathrm{m}^{-1}$ and a particle size parameter of unity. The scattering phase function curves of all the particles could be obtained from [19]. It can be noted that the anthracite is the best in terms of enhancing the radiation heat emitted from the hot wall while allows the maximum radiation heat to be transferred to biomass inside the two pyrolysis rooms. Moreover, it is stated that the medium anisotropy effect is the weakest for the fly ash due to its small imaginary part complex index of refraction, thus resulting in a more similar distribution of heat flux in the medium.

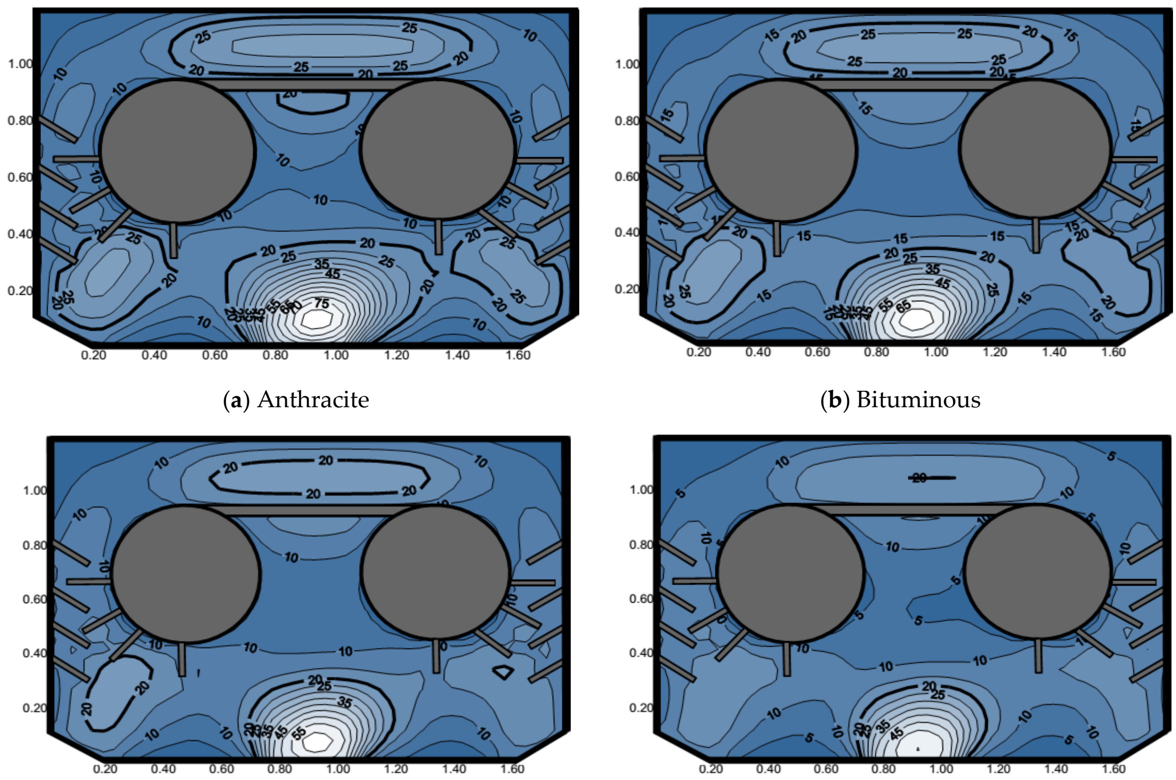

(**a**) Anthracite (**b**) Bituminous

(**c**) Lignite (**d**) Fly Ash

Figure 10. Isothermal profilesfor different particles materials at the plane z = 0.0 m (x_p = 1, ω = 0.9, κ = 5 m^{-1}). (**a**) Anthracite, (**b**) Bituminous, (**c**) Lignite, (**d**) Fly Ash.

Table 5 depicts the average temperature and net radiation heat flux for the four coal types and fly ash. It can be noted that the anthracite has the highest impact. The average temperature and net radiation heat flux increase is equal to 25.18% and 62.70% for the albedo coefficients of $\omega = 0.1$ and $\omega = 0.9$, respectively. All the considered coals and fly ash have similar trends as the carbon, because they almost lead to the same angular distribution of the scattered radiation.

Table 5. The average temperature and net radiation heat flux density value for different albedo values (κ = 1 m^{-1}).

Albedo		ω = 0.1	ω = 0.5	ω = 0.7	ω = 0.9
Anthracite	T_{Av} (K)	584.84	603.29	636.35	783.78
	q_{Av} (kW·m^{-2})	6.00	6.41	7.43	16.09
Bituminous	T_{Av} (K)	584.70	601.67	631.83	760.44
	q_{Av} (kW·m^{-2})	6.00	6.35	7.23	14.25
Lignite	T_{Av} (K)	584.51	599.4	625.18	729.51
	q_{Av} (kW·m^{-2})	5.99	6.27	6.97	12.09
Fly ash	T_{Av} (K)	584.33	597.41	619.45	703.79
	q_{Av} (kW·m^{-2})	5.98	6.20	6.75	10.53

Figure 11a,b illustrates the predictions of the radiation flux divergence along the centerline (0.9, 0.6, z) m for different particle materials ($x_p = 1$), an albedo coefficient $\omega = 0.9$ and two absorption coefficient values. It can be noted in Figure 11a that all the curves have the same shape and they are high in the center region. The radiation source term profiles follow the same trend as in [19]. Moreover, the difference between the highest value (for anthracite) and the lowest value (for fly ash) varies between 15.07% and 16.82% for $\kappa = 1$ m^{-1} and around 49% for the relatively optically thick medium ($\kappa = 5$ m^{-1}). Further radiation energy is transferred through the medium whereas the optical thickness is enhanced. The highest amount of the radiation flux divergence corresponds to the anthracite which is multiplied by a factor of 8, when increasing the absorption coefficient from $\kappa = 1$ to $\kappa = 5$ m^{-1}. This is might be due to the large value of the imaginary part of anthracite's complex index of refraction.

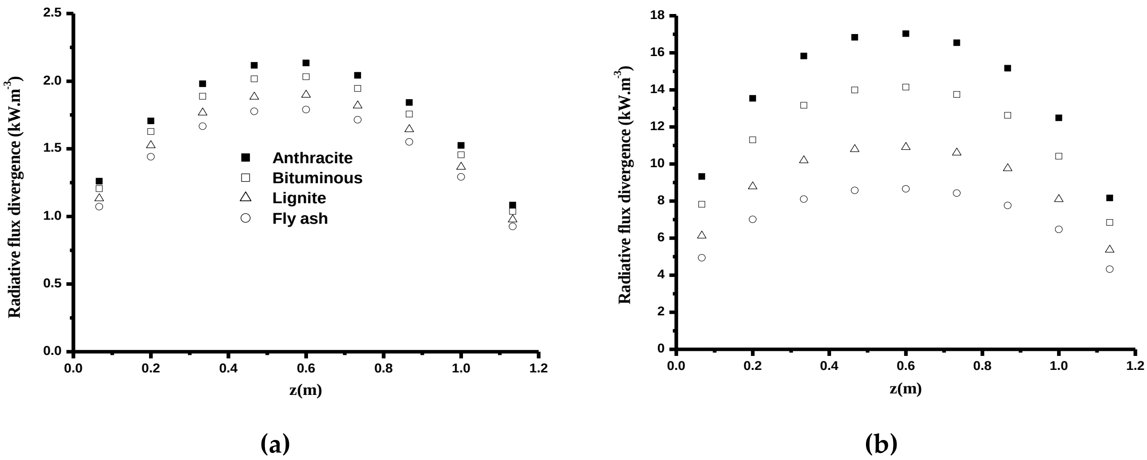

Figure 11. Profiles of the radiation flux divergence along the centerline for different particle materials (x_p = 1, ω = 0.9): (**a**) κ = 1 m^{-1}, (**b**) κ = 5 m^{-1}.

6.4. Particle Size Parameter Effect

Figure 12a,b demonstrates the predictions of the radiation heat flux for fly ash in y-direction, having various particle size parameters: (a) q_{yz} at the middle of the south hot surface along (0.9, 0.0, z) m and (b) q_{yx} at the middle of the north surface along (x, 1.2, 0.6) m with a purely scattering medium (ω = 1). The profiles of the involved phase functions are presented in Figure 2. One can easily notice that when the particle size parameter increases, the forward scattering behavior becomes more significant. According to Figure 12a, the largest radiation heat flux density, produced by the highest value of the particle size parameter. The radiation heat flux difference between the smallest and the largest particle size parameter is equal to 6.64%. While, in Figure 12b this difference is the largest at the location $x = 0.9$ m, (i.e., 6.67%). Approaching the ends, where the side baffles are located, the difference becomes more and more weak. The mean temperature calculated at the plane $z = 0$ varies between 585.56 K and 588.99 K, and the mean radiation heat flux varies between 6.64 kW·m^{-2} and 6.81 kW·m^{-2}. It is concluded that by increasing the size parameter, the evolution of the temperature and net radiation heat flux density transfer is imperceptible.

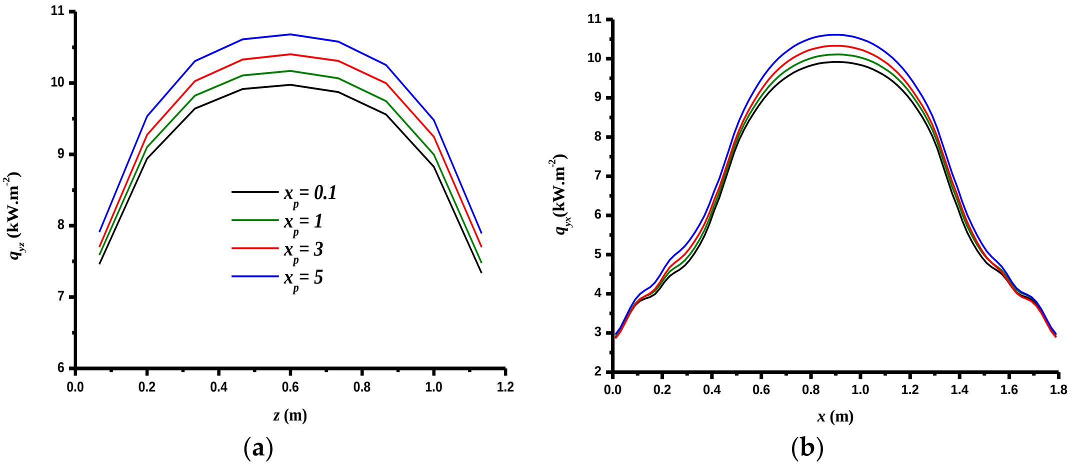

Figure 12. Profiles of the net predicted y-net radiation flux density for fly ash with different particle size parameters ($\omega = 0.9$, $\beta = 1$ m^{-1}): (**a**) (0.9, 0.0, z) m and (**b**) (x, 1.8, 0.6) m.

Figure 13 shows the impact of the fly ash particle size parameter on the radiation heat flux density q_{yx}, at the middle of the north wall, for different optical thicknesses. The anisotropic scattering effect is not considerable for $\beta = 1$, because it is compatible with a thin optical state without much scattering occurring. The effect of the particle size parameter is more pronounced for higher extinction coefficients, (i.e., $\beta = 10$). Moreover, when β increase, the radiation heat flux difference between the smallest and the largest particle size parameter become more important, mainly at the location $x = 0.9$ m where it reaches 13.84%.

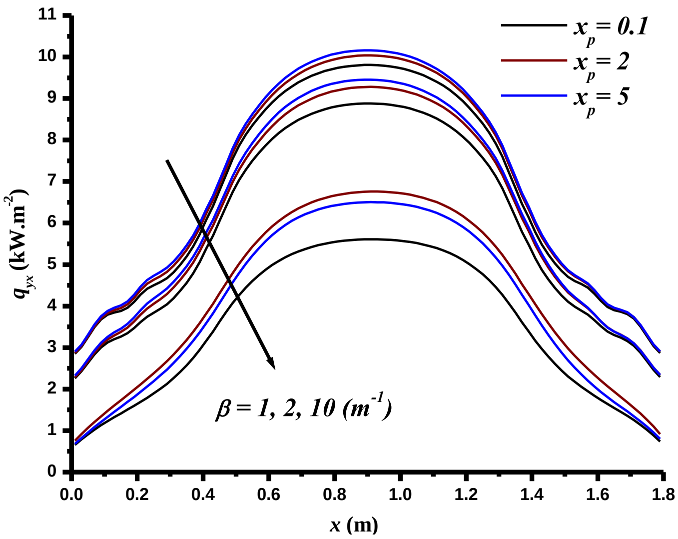

Figure 13. Evolution of the y-net radiation heat flux density component along (x, 1.8, 0.6) m vs the fly ash particle size parameter ($\omega = 0.5$).

7. Conclusions

In present research, the radiation heat transfer in a biomass pyrolysis pilot plant with an absorbing and anisotropic scattering medium is studied. The calculation procedure of the radiation transfer equation (RTE) is numerically done by coupling the Mie theory and the finite volume method (FVM) with the STEP scheme, using the blocked-off-region process. The numerical code was satisfactorily validated by comparison of the predictions with available data for a present work. The goal of present investigation is to study the anisotropic scattering phenomenon impact on the radiation heat transfer in the biomass pyrolysis pilot plant, and especially the two pyrolysis rooms. It is concluded that the anisotropic character of particles is negligible for small values of the albedo regardless the value of the absorption coefficient. When the albedo boosts, the net radiation heat flux diminishes for the forward and backward phase functions, and is underpredicted as compared to the isotropic case. This decrease is more important when the absorption coefficient changes from $\kappa = 1$ to $\kappa = 5$ m^{-1}. The predictions for solid particles of different coals and fly ash which are very similar to the actual combustion processes are produced. It is obtained that the net radiation heat flux enhances by the increment of the albedo coefficient. This tendency is similar for all the coals and fly ash, because these particles have almost the same angular distribution of the scattered radiation for low or moderate absorption coefficient values. In addition, it is found that the radiation energy transferred to biomass inside the two pyrolysis rooms is enhanced when using the anthracite's particles. The impact of the particle size parameter on the radiation heat flux for fly ash was analyzed. It is concluded that the net radiation heat flux enhances by increment of the particle size parameter. Furthermore, for high extinction coefficient values, a remarkable decrement in the net radiation heat flux is obtained, and the radiation heat flux difference between the smallest and the largest particle size parameter become more significant.

The numerical code developed and validated in the present investigation can further be extended to a 3-D configuration for a more pragmatic modeling of the heat transfer in the biomass pyrolysis pilot plant. Another possible perspective of the present work is to use the present code for the study of radiating nanoparticles in the flow of nanofluids by coupling the work like [29–33] and the present code.

Author Contributions: Conceptualization, M.A.A., M.M.S., and M.G.; methodology, A.E. and H.F.; software, K.G. and A.O.; validation, A.E., H.F. and M.N.B.; formal analysis, A.E.; investigation, H.F; resources, M.A.A.; data curation, K.G.; writing—original draft preparation, M.A.A. and A.E.; writing—review and editing, M.M.S. and M.G.; visualization, M.N.B.; supervision, M.M.A.; project administration, M.G.

Funding: This research received no external funding.

Conflicts of Interest: The authors declare no conflict of interest.

Nomenclature

a	coefficient of the discretized equations
b	source term of the discretized equations
D	direction cosines
E	radiation emissive power
I	radiant intensity
k	imaginarypart of the complex index
M	a large number (M = 10^{20})
m	complex index of refraction, face of control volume
N_θ	number of angular discretization in the polar angle
N_ϕ	number of angular discretization in the azimuthal angle
n	real part of the complex index of refraction or index in infinite series
P_n	Legendre Polynomial of order n
q	radiation heat flux
Q	efficiency factor

$\vec{r}$	position vector
r	particle radius
S	source function
S_{bloc}, S_C, S_P	additional source terms for blocked-off region procedure
s	distance in the direction $\vec{\Omega}$ of radiant intensity; curvilinear coordinate.
T	temperature
x_p	particle size parameter
x, y, z	Cartesian coordinates
Greek Symbols	
β	extinction coefficient
ΔA	area of a control volume face
ΔV	control volume
$\Delta\Omega$	control solid angle
ε	emissivity
κ	absorption coefficient
λ	wavelength of incident radiation
μ	direction cosine in the x-direction
ρ	reflectivity
θ	polar angle
Θ	scattering angle
σ	scattering coefficient
ϕ	azimuthal angle
Φ	phase function
$\overline{\Phi}^{l'l}$	average scattering phase function
ω	scattering albedo coefficient
$\vec{\Omega}$	angular direction
Subscript	
l, l′	angular directions
*	dimensionless
Av	average
b	blackbody
ext, sca, abs	extinction, scattering and absorption, respectively
e, w, n, s, r, f	east, west, north, south, rear and front neighbours of control volume P
E, W, N, S, B, T	nodes around the nodal point P
w	wall
Abbreviations	
RTE	radiation transfer equation
SPF	scattering phase function
WSGGM	weighted sum of gray gases model
ZM	zone method

References

1. Lockwood, F.C.; Shah, N.G. A new radiation solution method for incorporation in general combustion prediction procedures. *Symp. Int. Combust.* **1981**, *18*, 1405–1414. [CrossRef]
2. Malalasekera, W.M.G.; Lockwood, F.C. Computer Simulation of the King's Cross Fire: Effect of Radiative Heat Transfer on Fire. *Proc. Inst. Mech. Eng. Part C* **1991**, *205*, 201–208. [CrossRef]
3. Malalasekera, W.M.G.; James, E.H. Radiative Heat Transfer Calculations in Three Dimensional Complex Geometries. *J. Heat Transf.* **1996**, *118*, 225–228. [CrossRef]
4. Chai, J.C.; Lee, H.S.; Patankar, S.V. Treatment of Irregular Geometries Using a Cartesian-Coordinates-Based Discrete-Ordinates Method, Radiative Heat Transfer. *Theory Appl.* **1993**, *244*, 49–54.
5. Fivel, W.A.; Jesse, J.P. Finite Element Formulation of the Discrete-Ordinates Method for Multidimensional Geometries, Radiative Heat Transfer. *Curr. Res.* **1994**, *276*, 49–57.

6. Chai, J.C.; Parthasarathy, G.; Lee, H.S.; Patankar, S.V. Finite Volume Radiative Heat Transfer Procedure for Irregular Geometries. *J. Heat Transf.* **1995**, *9*, 410–415. [CrossRef]
7. Chai, J.; Lee, H.S.; Patankar, S.V. Treatment of irregular geometries using a Cartesian coordinates finite volume radiative heat transfer procedure. *Numer. Heat Transf. Part B* **1994**, *26*, 225–235. [CrossRef]
8. Borjini, M.N.; Farhat, H.; Radhouani, M.S. Analysis of radiative heat transfer in a partitioned idealized furnace. *Numer. Heat Transf. Part A* **2003**, *35*, 467–495. [CrossRef]
9. Guedri, K.; Borjini, M.N.; Farhat, H. Modelization of Combined Radiative and Conductive Heat Transfer in Three-Dimensional Complex Enclosures. *Int. J. Numer. Methods Heat Fluid Flow* **2005**, *15*, 257–276. [CrossRef]
10. Chai, J.C.; Moder, J.P. Spatial-Multiblock Procedure for Radiation Heat Transfer. *Numer. Heat Transf. B* **1997**, *31*, 277–293. [CrossRef]
11. Coelho, P.J.; GonÇalves, J.M.; Carvalho, M.G.; Trivic, D.N. Modeling of Radiative Heat Transfer in Enclosures with Obstacles. *Int. J. Heat Mass Transf.* **1998**, *41*, 745–756. [CrossRef]
12. Guedri, K.; Abbassi, M.A.; Borjini, M.N.; Halouani, K. Application of the finite-volume method to study the effects of baffles on radiative heat transfer in complex enclosures. *Numer. Heat Transf. Part A* **2009**, *55*, 1–27. [CrossRef]
13. Abbassi, M.A.; Guedri, K.; Borjini, M.N.; Halouani, K.; Zeghmati, B. Modeling of radiative heat transfer in 2D complex heat recuperator of biomass pyrolysis furnace: A study of baffles shadow and soot volume fraction effects. *Int. J. Math. Comput. Nat. Phys. Eng.* **2014**, *8*, 450–460.
14. Mengüç, M.P.; Viscanta, R. Radiative transfer in three-dimensional rectangular enclosures containing inhomogeneous, anisotropically scattering media. *J. Quant. Spectrosc. Radiat. Transf.* **1995**, *33*, 533–549. [CrossRef]
15. Kim, T.K.; Lee, H.S. Effect of anisotropic scattering on radiative heat transfer in two-dimensional rectangular enclosures. *Int. J. Heat Mass Transf.* **1988**, *31*, 1711–1721. [CrossRef]
16. Kim, T.K.; Lee, H.S. Radiative heat transfer in two dimensional anisotropic scattering media with collimated incidence. *J. Quant. Spectrosc. Radiat. Transf.* **1989**, *42*, 225–238. [CrossRef]
17. Farmer, J.T.; Howell, J.R. Monte Carlo Prediction of Radiative Heat Transfer in Inhomogeneous, Anisotropic, Nongray Media. *AIAA J. Thermophys. Heat Transf.* **1994**, *8*, 133–139. [CrossRef]
18. Guo, Z.; Maruyama, S. Scaling anisotropic scattering in radiative transfer in three-dimensional nonhomogeneous media. *Int. Commun. Heat Mass Transf.* **1999**, *26*, 997–1007. [CrossRef]
19. Trivic, D.N.; O'Brien, T.J.; Amon, C.H. Modeling the radiation of anisotropically scattering media by coupling Mie theory with finite volume method. *Int. J. Heat Mass Transf.* **2004**, *47*, 5765–5780. [CrossRef]
20. Trivic, D.N.; Amon, C.H. Modeling the 3-D radiation of anisotropically scattering media by two different methods. *Int. J. Heat Mass Transf.* **2008**, *51*, 2711–2732. [CrossRef]
21. Trivic, D.N. 3-D radiation modeling of nongray gases–particles mixture by two different numerical methods. *Int. J. Heat Mass Transf.* **2014**, *70*, 298–312. [CrossRef]
22. Hunter, B.; Guo, Z. Improved treatment of anisotropic scattering in radiation transfer analysis using the finite volume method. *Heat Transf. Eng.* **2015**, *37*, 341–350. [CrossRef]
23. Guedri, K.; Al-Ghamdi, A.S.; Bouzid, A.; Abbassi, M.A.; Ghulman, H.A. Evaluation of the FTn finite volume method for transient radiative transfer in anisotropically scattering medium. *Numer. Heat Transf. Part A* **2015**, *68*, 1137–1154. [CrossRef]
24. Chai, J.C.; Lee, H.S.; Patankar, S.V. Finite volume method for radiation heat transfer. *J. Heat Transf.* **1994**, *8*, 419–425. [CrossRef]
25. Chai, J.C.; Patankar, S.V. Finite-volume method for radiation heat transfer. In *Advances in Numerical Heat Transfer 2*; Minkowycz, W.K., Sparrow, E.H., Eds.; Taylor & Francis: Boca Raton, FL, USA, 2000.
26. Deirmendjian, D.; Clasen, R.; Viezee, V. Mie scattering with complex index of refraction. *J. Opt. Soc. Am.* **1961**, *51*, 620–633. [CrossRef]
27. Abbassi, M.A.; Grioui, N.; Halouani, K.; Zoulalian, A.; Zeghmati, B. A practical approach for modelling and control of biomass pyrolysis pilot plant with heat recovery from combustion of pyrolysis products. *Fuel Process. Technol.* **2009**, *90*, 1278–1285. [CrossRef]
28. Modest, M.F. *Radiative Heat Transfer*; Academic Press: New York, NY, USA, 2013.
29. Togun, H.; Safaei, M.R.; Sadri, R.; Kazi, S.N.; Badarudin, A.; Hooman, K.; Sadeghinezhad, E. Numerical simulation of laminar to turbulent nanofluid flow and heat transfer over a backward-facing step. *Appl. Math. Comput.* **2014**, *239*, 153–170. [CrossRef]

30. Hosseini, M.; Safaei, M.R.; Estellé, P.; Jafarnia, S.H. Heat transfer of water-based carbon nanotube nanofluids in the shell and tube cooling heat exchangers of the gasoline product of the residue fluid catalytic cracking unit. *J. Therm. Anal. Calorim.* **2019**, 1–12. [CrossRef]
31. Togun, H.; Ahmadi, G.; Abdulrazzaq, T.; Shkarah, A.J.; Kazi, S.N.; Badarudin, A.; Safaei, M.R. Thermal performance of nanofluid in ducts with double forward-facing steps. *J. Taiwan Inst. Chem. Eng.* **2015**, *47*, 28–42. [CrossRef]
32. Safaei, M.R.; Togun, H.; Vafai, K.; Kazi, S.N.; Badarudin, A. Investigation of heat transfer enhancement in a forward-facing contracting channel using FMWCNT nanofluids. *Numer. Heat Transf. Part A Appl.* **2014**, *66*, 1321–1340. [CrossRef]
33. Gholamalizadeh, E.; Pahlevanzadeh, F.; Ghani, K.; Karimipour, A.; Nguyen, T.K.; Safaei, M.R. Simulation of water/FMWCNT nanofluid forced convection in a microchannel filled with porous material under slip velocity and temperature jump boundary conditions. *Int. J. Numer. Methods Heat Fluid Flow* **2019**. [CrossRef]